Influence of the Coriolis force on the structure and evolution of wind turbine wakes

Mahdi Abkar*

Wind Engineering and Renewable Energy Laboratory (WiRE), École Polytechnique Fédérale de Lausanne (EPFL), 1015 Lausanne, Switzerland
and Center for Turbulence Research, Stanford University, Stanford, California 94305, USA

Fernando Porté-Agel†

Wind Engineering and Renewable Energy Laboratory (WiRE), École Polytechnique Fédérale de Lausanne (EPFL), 1015 Lausanne, Switzerland

(Received 7 March 2016; published 24 October 2016)

In this study, large-eddy simulation combined with a turbine model is used to investigate the effect of vertical wind veer associated with the Coriolis force on the structure and evolution of wind turbine wakes. In order to isolate the Coriolis effect on the wake, two cases are considered. In the first case, atmospheric boundary-layer flow is driven by a geostrophic wind, including the effect of Earth's rotation and the Coriolis force. In the second case, the boundary-layer flow is unidirectional and is forced by an imposed pressure gradient. Both cases have the same mean horizontal velocity and turbulence intensity at the hub height. The simulation results show that the Coriolis force significantly affects the aerodynamics of the wake including the mean velocity deficit, turbulence statistics, and wake-meandering characteristics downwind of the turbine. In particular, when the flow is forced by a geostrophic wind, vertical wind veer causes a skewed spatial structure in the wake. Moreover, the presence of lateral wind shear, in addition to the vertical one, enhances the shear production of turbulent kinetic energy and the turbulent momentum flux. This leads to a larger flow entrainment and, thus, a faster wake recovery compared to the case forced by unidirectional pressure gradient. Consistent with this result, wake meandering is also stronger in both lateral and vertical directions in the case of geostrophic forcing compared to the case with pressure-gradient forcing.

DOI: 10.1103/PhysRevFluids.1.063701

I. INTRODUCTION

Wind turbines operate in the lowest part of the atmospheric boundary layer (ABL), where they are exposed to different levels of wind shear, thermal stratification, and turbulence. As reported in several studies [1–5], these ABL characteristics, which in fact vary on daily and seasonal cycles [6], have significant impacts on the structure and evolution of wind turbine wakes and their mutual interactions within a wind farm. Because wind turbine wakes are the main cause of power losses inside a wind farm [7–12], detailed understanding and accurate prediction of wind turbine wakes under different incoming ABL flow conditions are needed in order to design more efficient and more reliable wind farms.

Much work, including laboratory experiments, field-scale measurements, and numerical simulations, has been done recently to study the effects of different incoming flow conditions on the aerodynamics of wind turbine wakes. Some studies have addressed the effect of mean wind shear in the incoming wind on the structure of wind turbine wakes. One of the main outcomes of these studies is that, in the absence of mean wind shear in the incoming wind (uniform inflow condition),

*abkar@stanford.edu
†fernando.porte-agel@epfl.ch

mean velocity and turbulence statistics are nearly axisymmetric [13–15]. However, for a wind turbine sited in a boundary layer, nonaxisymmetric behavior of the wake has been observed in response to the nonuniform incoming flow and the effect of the ground. In particular, the shear production of turbulent kinetic energy is higher in the upper edge of the wake, due to the higher wind shear and turbulent fluxes in that region [16–23]. In addition, it has been shown that the presence of the ground, combined with the vertical gradient of velocity in the ABL, limits wake meandering in the vertical direction compared to the horizontal one [24–26]. Some other studies have investigated the impact of atmospheric turbulence, created by either different land-surface covers or different thermal stratifications, on wind turbine wakes. Specifically, both numerical simulations [13,18,26–34] and experimental studies [16,35–45] have shown that stand-alone turbine wakes recover faster in conditions with higher turbulence levels in the incoming flows. This is mainly related to the fact that the higher turbulence levels, associated with either higher aerodynamic surface roughnesses or positive buoyancy under convective conditions, lead to a larger flow entrainment and, thus, a faster wake recovery. In addition, it has been found that the meandering of the wake, in both lateral and vertical directions, is also enhanced by increasing the turbulence level of the incoming wind [25,26,46].

Among the aforementioned studies, the ones that are based on wind tunnel experiments or numerical simulations using pressure-gradient forcing are limited to the unidirectional incoming wind condition and cannot account for vertical wind veer associated with the Coriolis effect. As a result of the Coriolis force associated with planetary rotation, the wind direction changes with height, resulting in a lateral shear in addition to the vertical shear. This effect is much stronger at night, under stably stratified conditions, where the boundary layer is very shallow [47]. The effect of this phenomenon on wind turbine wakes was first shown by Magnusson and Smedman [37] in a field-scale experiment. They showed that under the stable conditions, the velocity deficit downwind of the turbine is skewed and tilted to one side with height. Later, Zahle *et al.* [48] performed one of the first numerical investigations to study the influence of lateral shear on wind turbine wakes using the Reynolds-averaged Navier-Stokes (RANS) technique. They showed that for the incoming flow with large lateral shear, the wake is skewed strongly, and it develops in a highly three-dimensional manner (highly asymmetric). Lu and Porté-Agel [49] employed large-eddy simulation (LES) to study wind turbine wakes inside an infinite wind farm in a stable boundary layer. They also showed that lateral shear induced by the Coriolis force causes a skewed spatial structure and drives a part of the turbulence energy away from the center of the wake. The skewed spatial structure of the wake due to directionally sheared inflow was further reported in some other studies using numerical simulations and field experiments [31–34,50–52].

All these studies specifically showed that for wind turbines, whose rotor diameters are on the order of 100 m, the effects of the lateral shear can be far from negligible. Since all turbine wakes in the ABL are subjected to the Coriolis force, it is of great importance to quantify the impact of veering incoming wind, compared to a unidirectional one, on wake characteristics such as wake recovery and wake meandering. In this regard, we use a recently developed LES framework to address the Coriolis effect on the development of turbine wakes. Note that this study can also serve as an assessment of the ability of wind tunnel studies, in which the Coriolis forcing cannot yet be included, to adequately represent important atmospheric effects on wind turbine wakes.

This paper is organized as follows. A short introduction of the LES framework is given in Sec. II. Section III presents the numerical setup and the LES results for the precursor simulations in the absence of wind turbines. The results obtained from the LES of wind turbine wakes are shown and discussed in Sec. IV. Finally, a summary and conclusions are provided in Sec. V.

II. LES FRAMEWORK

In this study, we use a modified version of the LES code which has been validated and used in previous wind energy studies (e.g., [49,51,53–56]). The code solves the filtered continuity equation, the filtered momentum conservation equations, and the filtered transport equation for the potential temperature, derived based on the Boussinesq approximation [57]:

$$\frac{\partial \tilde{u}_i}{\partial x_i} = 0,$$
$$\frac{\partial \tilde{u}_i}{\partial t} + \tilde{u}_j \frac{\partial \tilde{u}_i}{\partial x_j} = -\frac{\partial \tilde{p}^*}{\partial x_i} - \frac{\partial \tau_{ij}^d}{\partial x_j} + \delta_{i3} g \frac{\tilde{\theta} - \langle \tilde{\theta} \rangle}{\theta_0} - \frac{f_i}{\rho} + \mathcal{F}_i, \tag{1}$$
$$\frac{\partial \tilde{\theta}}{\partial t} + \tilde{u}_j \frac{\partial \tilde{\theta}}{\partial x_j} = -\frac{\partial q_j}{\partial x_j},$$

where the tilde represents spatial filtering operation at scale $\tilde{\Delta}$; t is the time; and x_i is the ith axis in Cartesian coordinates [with $i = 1,2,3$ corresponding to the streamwise (x), spanwise (y), and vertical (z) directions, respectively]. $(\tilde{u}_1,\tilde{u}_2,\tilde{u}_3) = (\tilde{u},\tilde{v},\tilde{w})$ are the components of the velocity field, and $\tilde{\theta}$ is the filtered potential temperature. θ_0 is the reference temperature. The angle brackets denote a horizontal average, and δ_{ij} is the Kronecker delta tensor. g is the gravitational acceleration, and ρ is the fluid density. τ_{ij}^d is the deviatoric part of the subgrid-scale (SGS) stress tensor ($\tau_{ij} = \widetilde{u_i u_j} - \tilde{u}_i \tilde{u}_j$), and $q_j = \widetilde{u_j \theta} - \tilde{u}_j \tilde{\theta}$ is the SGS heat-flux vector. $\tilde{p}^* = \tilde{p}/\rho + \frac{1}{3}\tau_{kk}$ is the modified pressure, where $\tilde{p}$ is the deviation of the pressure from the mean imposed pressure field, and τ_{kk} is the isotropic part of the SGS stress tensor. f_i is a body force (per unit volume of air) for modeling the effect of wind turbines on the flow, and $\mathcal{F}_i$ is a forcing term.

Since the Reynolds number of the ABL is very high, no near-ground viscous processes are resolved, and the viscous term is neglected in the momentum equation. In the simulations, the SGS turbulent fluxes are parametrized using Lagrangian scale-dependent dynamic models [58]. The turbine-induced forces are modeled using the rotating actuator-disk approach [53,55,59]. Unlike the standard actuator-disk approach, the rotating actuator-disk model takes into account the effects of turbine-induced flow rotation and nonuniform distribution of forces [60]. Through this model, the turbine blades are divided into N blade elements in the radial direction. The aerodynamic forces acting on each blade element are determined using the lift and drag characteristics of the airfoil type, as well as the local flow conditions. More details on the numerical method of the LES code is provided in the Appendix.

III. PRECURSOR SIMULATION

To generate the inflow conditions for the wind turbine wake simulations, two sets of simulations of the stable boundary layer without wind turbines are performed. The domain size is 1600 m $\times$400 m $\times$400 m, discretized into 160 $\times$ 80 $\times$ 80 grid points. For the first set of simulations, we chose the standard Gewex Atmospheric Boundary Layer Study (GABLS) case, which has been well established and tested with LES [61]. This case represents a typical quasiequilibrium moderately stable boundary layer, similar to those commonly observed over polar regions and equilibrium nighttime conditions over land in midlatitudes.

In summary, the ABL flow is driven by geostrophic wind and includes the effect of Earth's rotation and the Coriolis force. In this case, the forcing term in Eq. (1) is defined as $\mathcal{F}_i = f_c \varepsilon_{ij3}(\tilde{u}_j - G_j)$, where f_c is the Coriolis parameter and is set to $f_c = 1.39 \times 10^4$ rad/s (corresponding to latitude 73°N), ε_{ijk} is the alternating unit tensor, and G is the geostrophic wind with a magnitude of 8 m/s. The simulations are initialized with a constant streamwise velocity of 8 m/s and zero velocity for the spanwise and vertical components. The initial potential temperature profile consists of a mixed layer (with potential temperature 265 K) up to 100 m with an overlying inversion of strength 10 K/km, and the surface (ground level) potential temperature is reduced at a prescribed surface cooling rate of 0.25 K/h. The surface roughness length for momentum and heat is set to 0.1 m, and the reference potential temperature is $\theta_0 = 263.5$ K. The simulation attains a quasisteady state in 8–9 h [61]. Therefore, the instantaneous velocity and potential temperature fields during the last hour of simulation are saved and then used as inflows to the wind turbine wake simulations. It should

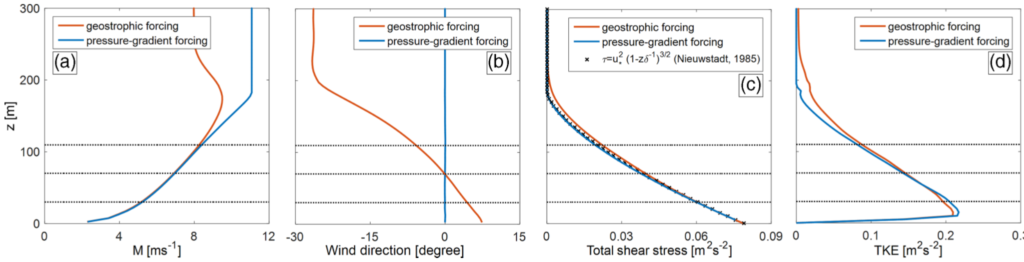

FIG. 1. Vertical profiles of (a) horizontally averaged velocity magnitude (m s^{-1}), (b) wind direction (degree), (c) total shear stress (m^2 s^{-2}), and (d) TKE (m^2 s^{-2}) of the incoming ABL flows. The horizontal dotted lines show the top-tip, hub, and bottom-tip heights.

be noted that as a result of the Coriolis force in the momentum equations, wind direction inside the ABL changes with height in a way that is not known *a priori*. Hence, it should be ensured that the mean velocity direction is always aligned with the turbine axes at the hub-height level. To do so, a control algorithm is used, in which a gradual adjustment of the geostrophic wind is applied by adding a source term in the momentum equations. A similar algorithm has been used recently [51,62–64] in the simulation of ABL flows through wind farms under different atmospheric stability regimes.

In this study, in order to isolate the effect of wind veer on the evolution of wind turbine wakes, another simulation is performed in which the flow is unidirectional and driven by an imposed pressure gradient. In this case, we specify the forcing term ($\mathcal{F}_i$), the surface heat flux ($q_3|_w$), and the boundary layer height (δ) (i.e., the height at which the total momentum flux reaches 5% of the surface value [65]) such that both simulations have the same mean horizontal velocity and turbulence intensity at the hub height. In particular, the forcing term is defined as $\mathcal{F}_i = \frac{3}{2}u_*^2/\delta(1-z/\delta)^{1/2}\delta_{i1}$, and is obtained from Nieuwstadt's steady-state one-dimensional model for prediction of the total shear stress in the stable boundary layer [66,67]. This model assumes the momentum flux normalized by its respective surface value follows z/δ to the $3/2$ power. For the second set of simulations, u_*, $q_3|_w$, and δ are set equal to the ones obtained from the GABLS case.

The main characteristics of the simulated ABLs with different forcing terms are shown in Fig. 1. Vertical profiles of the horizontally averaged velocity magnitude and wind direction are shown in Figs. 1(a) and 1(b). As seen in these figures, both cases have the same mean horizontal velocity at the hub height. However, in the case of flow forced by geostrophic wind, the direction of the wind changes with height due to the effect of the Coriolis force in the momentum equations. For the particular case considered in this study, the change of wind direction from the surface to the top of the boundary layer is around 33°, which is in good agreement with most real conditions and with the simulation results of many stable boundary layers, including the GABLS case [61,68–71]. Figures 1(c) and 1(d) show the vertical profiles of the total shear stress and turbulent kinetic energy (TKE) for both cases. The prediction of the total shear stress using the model proposed by Nieuwstadt [66,67] is also plotted in Fig. 1(c) for comparison. As observed in these figures, both cases have almost the same turbulent momentum flux and TKE throughout the boundary layer.

IV. WIND TURBINE WAKE SIMULATION

The simulated ABL flows using the two different forcing terms in the absence of wind turbines are used as inflows to investigate the effects of vertical wind veer on wind turbine wakes. In the simulations, Vestas V80-2MW wind turbines with a rotor diameter (D) of 80 m and a hub height (z_h) of 70 m are immersed in the flow. More details on the turbine characteristics can be found in [59]. In should be noted that, to avoid the downwind flow affecting the flow upwind of the turbine due to the periodic boundary conditions, a buffer zone is applied to smoothly adjust the flow from the very-far-wake downwind condition to that of the precursor simulation [60,72–74].

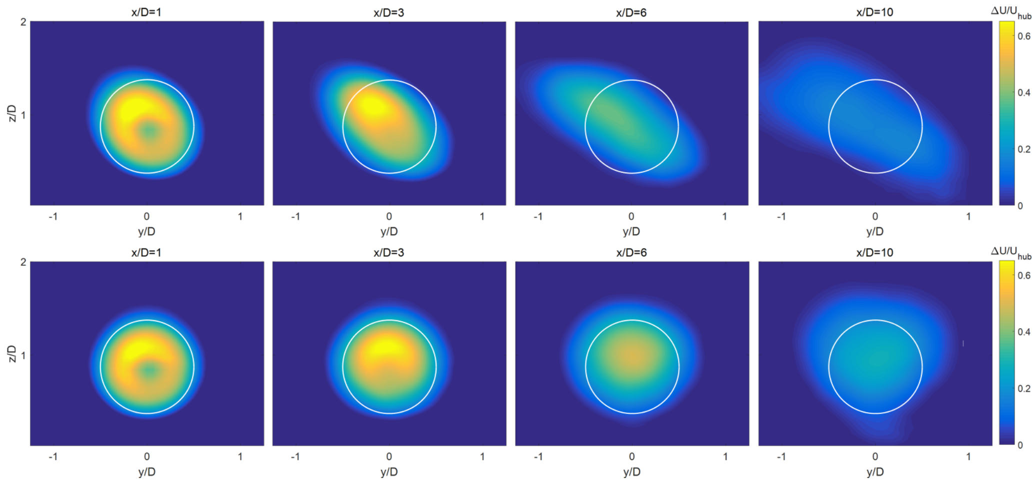

FIG. 2. Contour plots of the normalized velocity deficit in the vertical y-z planes at $x/D = 1, 3, 6$, and 10 downwind of the turbine for (top) geostrophic forcing and (bottom) pressure-gradient forcing. The white circle shows the location of the turbine.

A. General characteristics of the wake: Mean velocity deficit and turbulence intensity

Figure 2 shows two-dimensional fields of the normalized velocity deficit ($\Delta U/U_{\text{hub}}$) in the lateral cross-sectional planes at $x/D = 1, 3, 6$, and 10 downwind of the turbines, where $\Delta U = U_{\text{inflow}} - U$ is the mean velocity deficit, and U_{inflow} is the mean streamwise inflow velocity. As seen in this figure, when the incoming wind is unidirectional, the wake is almost symmetric with respect to the vertical axis. However, in the case of geostrophic forcing, the wake is strongly skewed owing to the strong cross flow component in the incoming wind. Similar behavior in the wake structure has been reported in previous numerical simulations and field-scale experiments of wind turbine wakes under stably stratified conditions [31–34,37,49–51].

Figure 3 shows the maximum velocity deficit with downwind distance for both cases. As seen in this figure, under veering incoming wind, not only is the wake skewed, but also it recovers faster compared to the case with unidirectional incoming flow. To better quantify the recovery of the wake downwind of the turbine, the following procedure is applied: for each distance downwind of the turbine, a multivariate Gaussian function is fitted to the normalized velocity deficit field. By using this method, we can compute the standard deviations of the Gaussian function along the principle axes of the wake (i.e., $\sigma_{y'}$ and $\sigma_{z'}$), and consequently, the equivalent standard deviation $\sigma_{\text{eq}} = \sqrt{\sigma_{y'}\sigma_{z'}}$, the ratio between them ($\sigma_{y'}/\sigma_{z'}$), and the rotation of the wake relative to the vertical axis (α) [see Fig. 4(a)]. Figures 4(b)–4(d) show the variation of the above-mentioned quantities with downwind

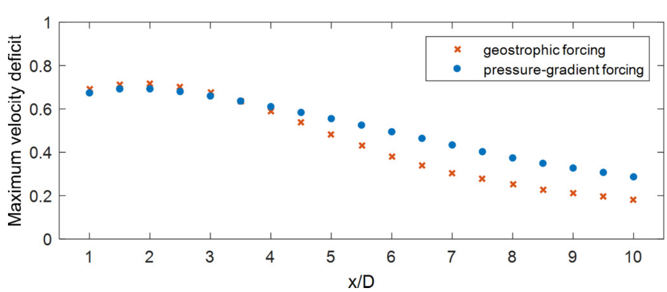

FIG. 3. Maximum velocity deficit with downwind distance.

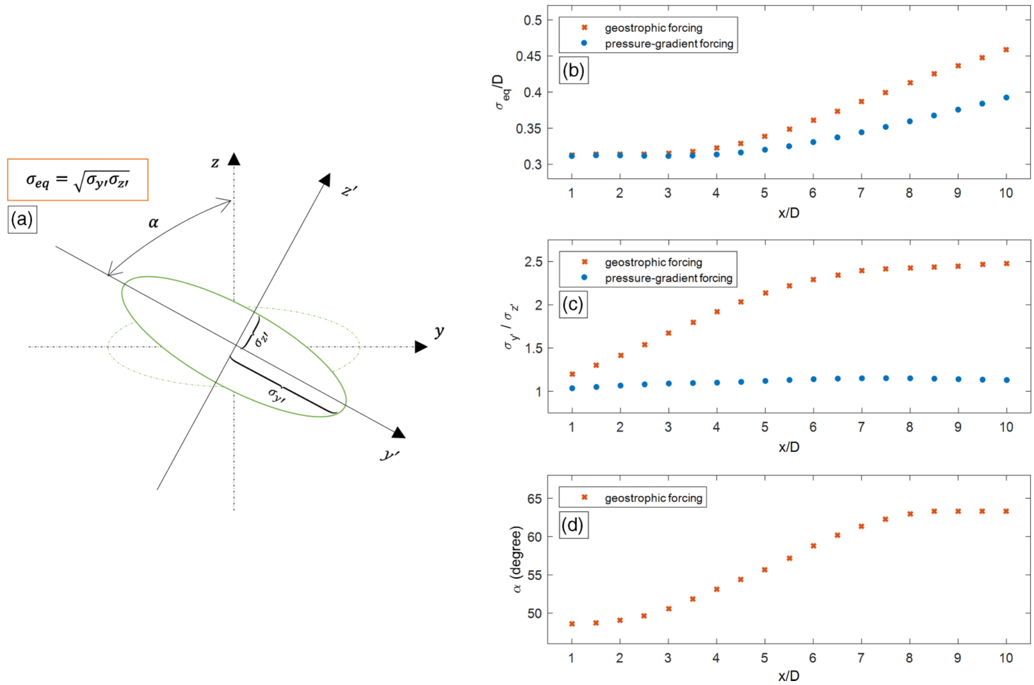

FIG. 4. (a) Schematic of the skewed wake, (b) normalized standard deviation of the velocity deficit (σ_{eq}/D), (c) $\sigma_{y'}/\sigma_{z'}$, and (d) the rotation of the wake (α) with downwind distance.

distance. As shown in Fig. 4(b), although the turbulence level of the incoming wind, shown in Fig. 1(d), is almost the same for both cases, the recovery of the wake is much faster in the case of flow forced by geostrophic wind. It is also observed that under geostrophic forcing condition, the ratio of $\sigma_{y'}$ to $\sigma_{z'}$ and the rotation of the wake (α) increase with downwind distance. The underlying reason is that, as a result of lateral shear in the incoming wind, the wake is stretched continually as it is transported downstream, which leads to an increase in the magnitude of $\sigma_{y'}/\sigma_{z'}$ and α. In contrast, in the case of unidirectional incoming wind, the ratio between $\sigma_{y'}$ and $\sigma_{z'}$ is almost constant regardless of the downwind distance with a larger value for the lateral expansion of the wake ($\sigma_{y'}$). Faster wake recovery in the lateral direction compared to the vertical one has been also reported in previous numerical studies of stand-alone wind turbine wakes [26,75].

Besides the velocity deficit, the enhancement of turbulence intensity is the other critical aerodynamic factor in wind turbine wakes that is highly related to failure of wind turbine components [76]. Figure 5 displays contour plots of the turbulence intensity in the lateral cross-sectional planes at $x/D = 1$, 3, 6, and 10 downwind of the turbine. The turbulence intensity (I_T) is computed as $I_T = \sqrt{2\tilde{k}/3}/U_{\text{hub}}$, where $\tilde{k}$ is the resolved turbulent kinetic energy. As seen in this figure, and in agreement with previous studies of wind turbine wakes in shear flows (e.g., [16,20,26,53]), the turbulence intensity is larger in the upper half of the wake, which is related to the intense production of TKE associated with the strong shear in that region. However, in the case of flow forced by geostrophic wind, large amount of turbulence is transported away from the center of the wake due to the lateral wind shear induced by the Coriolis force. It is also observed that, although the turbulence intensity of the incoming wind is similar for both cases, the turbulence intensity in the wake region is larger under geostrophic wind forcing. This higher turbulence level in the wake region contributes to larger flow entrainment and, consequently, a faster recovery of the wake than under unidirectional pressure-gradient forcing [Figs. 3 and 4(b)].

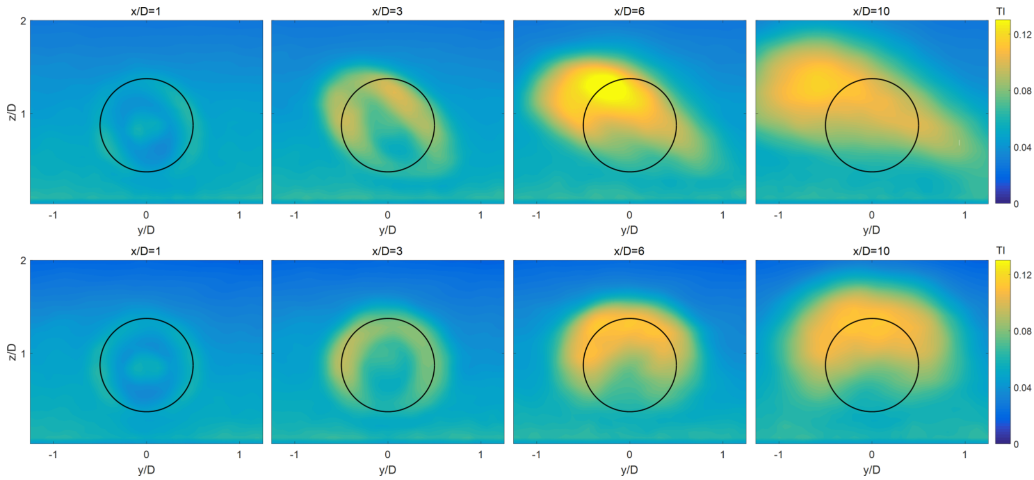

FIG. 5. Contour plots of turbulence intensity (TI) in the vertical y-z planes at $x/D = 1$, 3, 6, and 10 downwind of the turbine for (top) geostrophic forcing and (bottom) pressure-gradient forcing. The black circle shows the location of the turbine.

B. Kinetic energy budgets of the mean flow

To better understand the role of vertical wind veer on energy exchanges between the incoming ABL flow and wind turbine wakes, we carried out a detailed analysis of the mean kinetic energy budgets inside the wake. By performing time averaging on Eq. (1), one can write

$$\frac{\partial \bar{\tilde{u}}_i}{\partial t} + \bar{\tilde{u}}_j \frac{\partial \bar{\tilde{u}}_i}{\partial x_j} = -\frac{\partial \left(\bar{\tau}^d_{ij} + \overline{\tilde{u}'_i \tilde{u}'_j}\right)}{\partial x_j} + \delta_{i3} g \frac{\bar{\tilde{\theta}} - \langle \bar{\tilde{\theta}} \rangle}{\theta_0} - \frac{\bar{f}_i}{\rho} + \bar{\mathcal{F}}_i, \tag{2}$$

where the overbar denotes temporal averaging. An equation for the kinetic energy of the mean flow can be obtained by the product of Eq. (2) with $\bar{\tilde{u}}_i$ as follows:

$$\underbrace{\frac{\partial \bar{\tilde{K}}}{\partial t}}_{\substack{\text{Storage}\\ \approx 0}} + \underbrace{\bar{\tilde{u}}_j \frac{\partial \bar{\tilde{K}}}{\partial x_j}}_{\text{Adv.}} = \underbrace{-\frac{\partial \bar{\tilde{u}}_i \left(\bar{\tau}^d_{ij} + \overline{\tilde{u}'_i \tilde{u}'_j}\right)}{\partial x_j}}_{T_t} + \underbrace{\left(\bar{\tau}^d_{ij} + \overline{\tilde{u}'_i \tilde{u}'_j}\right) \frac{\partial \bar{\tilde{u}}_i}{\partial x_j}}_{-P_s} + \underbrace{\bar{\tilde{u}}_i \delta_{i3} g \frac{\bar{\tilde{\theta}} - \langle \bar{\tilde{\theta}} \rangle}{\theta_0}}_{-P_\theta} \underbrace{- \frac{\bar{\tilde{u}}_i \bar{f}_i}{\rho}}_{W_t} + \underbrace{\bar{\tilde{u}}_i \bar{\mathcal{F}}_i}_{W_G}, \tag{3}$$

where $\bar{\tilde{K}} = \frac{1}{2} \bar{\tilde{u}}_i \bar{\tilde{u}}_i$ is the mean kinetic energy, T_t denotes the transport of the mean kinetic energy by turbulence, P_s is the shear production, P_θ is the buoyancy production or suppression, W_t is the work done by the turbine, and W_G is the work done on the boundary layer by the forcing term [77,78].

In this study, we focus on the first two terms on the right-hand side of Eq. (3) in order to investigate the effect of vertical wind veer on turbulence production and the transport of mean kinetic energy into the wake. Figure 6 displays contour plots of the total turbulence production ($P_t = P_s + P_\theta$) in the lateral cross-sectional plane at $x/D = 1$, 3, 6, and 10 downwind of the turbine. As seen in this figure, the turbulence production is larger under geostrophic wind forcing than under pressure-gradient forcing. This is mainly related to the fact that the presence of lateral shear, in addition to the vertical shear in the incoming ABL wind, enhances the shear production of turbulent kinetic energy. The contribution of lateral wind shear in the total TKE production [i.e., $P_{23} = -(\bar{\tau}^d_{23} + \overline{\tilde{u}'_2 \tilde{u}'_3})(\partial \bar{\tilde{u}}_2 / \partial x_3)$] is also shown in Fig. 7. As clearly observed in this figure, when the flow is unidirectional, the contribution of lateral shear on TKE production is almost zero. However, in the case of veering incoming wind, the lateral wind shear significantly contributes to the total shear production and enhances the turbulence downwind of the turbine. The enhancement of turbulence due to the lateral wind shear under veering incoming wind leads to a larger mean kinetic energy

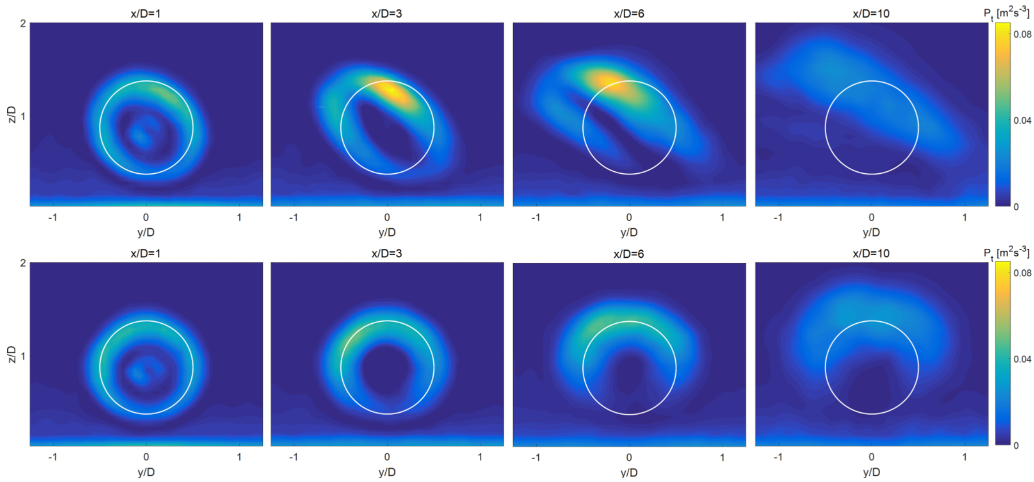

FIG. 6. Contours of total TKE production, P_t, in the vertical y-z planes at $x/D = 1$, 3, 6, and 10 downwind of the turbine for (top) geostrophic forcing and (bottom) pressure-gradient forcing. The white circle shows the location of the turbine.

entrainment and, thus, a faster wake recovery compared to the case under unidirectional incoming flow. This result is displayed in Fig. 8.

Regarding the other terms in Eq. (3), it should be noted that downwind of the turbine in the wake region, W_t is zero, since the local turbine-induced forces are zero at that location. Also, W_G is very small compared to the transport and production terms (not shown here). Hence, the advection term would be approximately balanced by the sum of the transport and production terms.

C. Wake-meandering characteristics

In this section, the LES data is used to study the effect of vertical wind veer in the incoming wind on wake meandering. The magnitude of wake meandering downwind of the turbine is determined as the standard deviation of the wake-center position in the lateral and vertical directions. In this

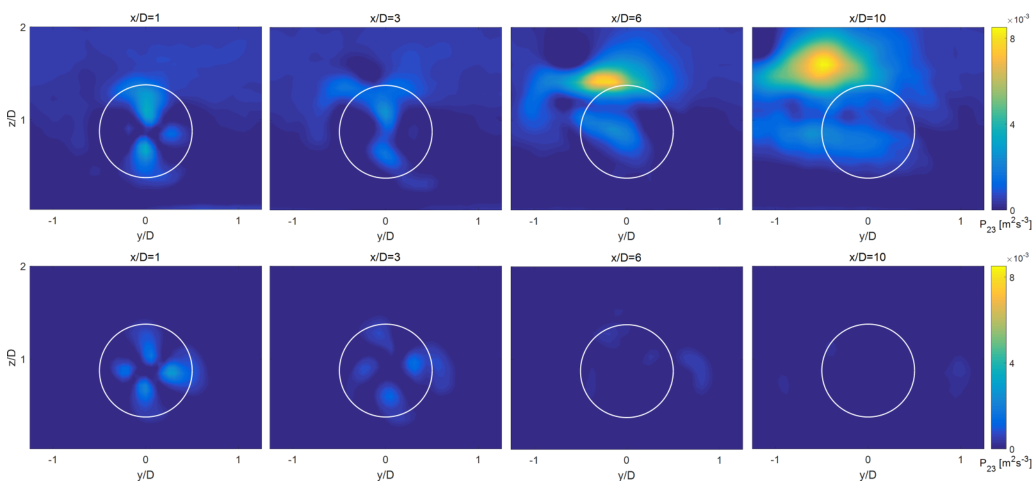

FIG. 7. Contours of the contribution of lateral shear on TKE production, P_{23}, in the vertical y-z planes at $x/D = 1$, 3, 6, and 10 downwind of the turbine for (top) geostrophic forcing and (bottom) pressure-gradient forcing. The white circle shows the location of the turbine.

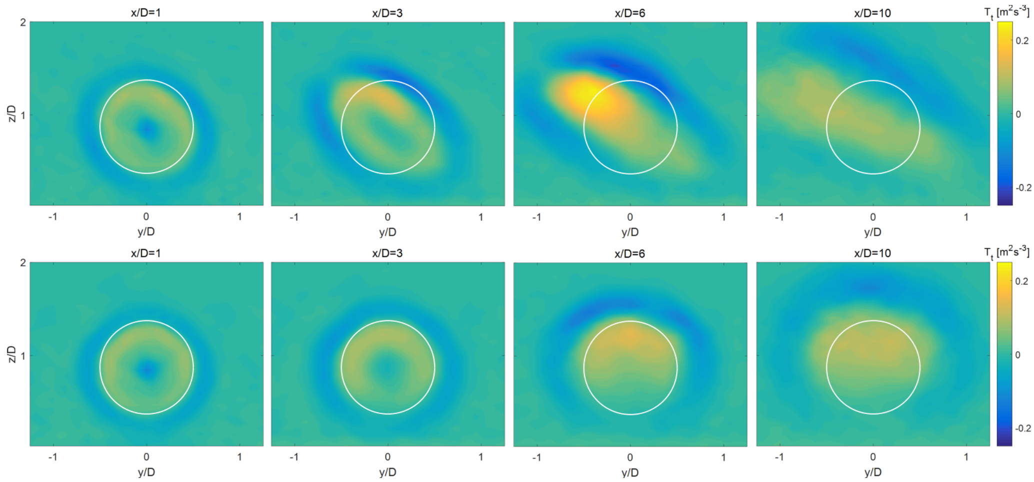

FIG. 8. Contours of mean kinetic energy transport into the wake, T_t, in the vertical y-z planes at $x/D = 1$, 3, 6, and 10 downwind of the turbine for (top) geostrophic forcing and (bottom) pressure-gradient forcing. The white circle shows the location of the turbine.

study, the instantaneous wake center at each lateral cross-sectional plane is defined as the center of momentum deficit, and it is computed as follows:

$$y_c(t) = \frac{\int \Delta\tilde{u}^2(t,y,z)y\,dy\,dz}{\int \Delta\tilde{u}^2(t,y,z)\,dy\,dz}, \quad z_c(t) = \frac{\int \Delta\tilde{u}^2(t,y,z)z\,dy\,dz}{\int \Delta\tilde{u}^2(t,y,z)\,dy\,dz}, \tag{4}$$

where $\Delta\tilde{u}(t,y,z) = U_{\text{inflow}}(y,z) - \tilde{u}(t,y,z)$.

Figure 9(a) shows the normalized standard deviation of the instantaneous wake center in the lateral and vertical directions as a function of downstream position. As seen in this figure, for both cases, wake meandering is weaker in the vertical direction than in the lateral one. This is mainly related to the fact that the presence of the ground together with the vertical gradient of the velocity in the ABL limit the wake meandering in the vertical direction. In addition, in these simulations, the stable stratification also reduces the vertical motions and, consequently, constrains the vertical movement of the wake. It is also observed that the wake meandering in both lateral and vertical directions is larger under the geostrophic forcing condition. This is despite the fact that, as shown in Figs. 9(b) and 1(d), the integral length scale and the turbulence level of the incoming ABL flows are nearly the same in both cases. It is worth mentioning that the integral length scales were calculated by applying the autocorrelation method on the time series of the velocity field at $x/D = -2$ upwind

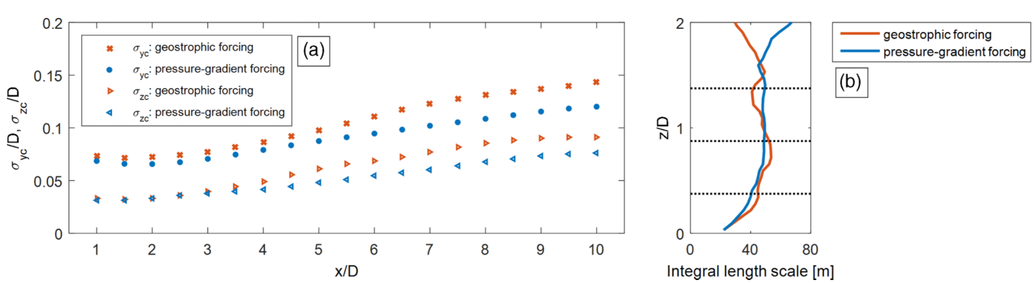

FIG. 9. (a) Standard deviation of the wake center normalized with the rotor diameter D in the lateral and vertical directions and (b) vertical profile of the integral length scale (m) at $x/D = -2$ upwind of the turbine for both cases.

of the turbine [24,79]. These results indicate that vertical wind veer should be taken into account, in addition to mean wind shear and turbulence levels, to describe the wake-meandering characteristics downwind of the turbine.

V. CONCLUSION

In this study, LES combined with the actuator-disk model is used to study the effect of vertical wind veer associated with the Coriolis force on the aerodynamics of wind turbine wakes. In the simulations, tuning-free Lagrangian scale-dependent dynamic models are used to model the SGS fluxes, while the turbine-induced forces (e.g., lift and drag) are parametrized with the rotating actuator-disk model. To isolate the Coriolis effect on the wake characteristics, two cases are simulated. In the first case, the ABL flow is driven by a geostrophic forcing that includes the effect of the Earth's rotation, while the second case considers the ABL flow as unidirectional, forced by an imposed pressure gradient. Both cases have the same mean horizontal velocity and turbulence level at the hub height.

The simulation results show that the Coriolis force has a significant effect on the structure and evolution of wind turbine wakes. In particular, the wind veer produced by the Coriolis force causes a strong skewed spatial structure in the wake. Moreover, the presence of the lateral wind shear in addition to the vertical one, enhances the shear production and turbulent kinetic energy in the wake region, leading to a larger flow entrainment and, thus, a faster wake recovery compared to the case with unidirectional incoming wind. It also found that, although the integral length scale of the incoming wind is almost the same for both cases, the enhancement of turbulence inside the wake due to the lateral wind shear under geostrophic wind conditions leads to a stronger wake meandering downwind of the turbine. These results show that, besides the mean wind shear and turbulence levels, vertical wind veer should be also taken into account to describe the dynamic of the wakes, specially in lower-order models such as analytical models. In addition, these simulation data indicate that the interpretation of the results obtained solely from thermally stratified wind tunnel boundary layers is not enough to guide actual wind farm design, since some atmospheric effects such as Coriolis forcing cannot yet be included.

ACKNOWLEDGMENTS

This research was supported by the Swiss National Science Foundation (Grants No. 200021-132122 and No. 206021-144976), the Swiss Federal Office of Energy (Grant No. SI/501337-01), and the Swiss Innovation and Technology Committee (CTI) within the context of the Swiss Competence Center for Energy Research "FURIES: Future Swiss Electrical Infrastructure". M.A. is also grateful to the Swiss National Science Foundation for its Postdoctoral Fellowship support.

APPENDIX: NUMERICAL METHOD

A numerical solution of Eq. (1) is obtained by discretizing the computational domain into N_x, N_y, and N_z uniformly spaced grid points with the resolution of Δ_x, Δ_y, and Δ_z in the streamwise, spanwise, and wall-normal directions, respectively. A staggered grid is used in the vertical direction, with the first vertical velocity plane on the surface, and the first horizontal velocity and potential temperature plane $\Delta_z/2$ from the surface. The vertical derivatives are approximated with second-order central differences, while the horizontal directions are discretized pseudospectrally. Full dealiasing of the nonlinear terms is performed in Fourier space according to the $3/2$ rule [80]. The LES equations are integrated in time using a second-order Adams-Bashforth method [81]. In the horizontal directions, the periodic boundary conditions are implicitly imposed. The upper boundary condition for the momentum conservation equations consists of a stress-free condition, besides a zero vertical velocity. The temperature gradient at the top of the domain is set to a constant lapse rate Γ, which is prescribed in the initial conditions. At the bottom surface, the instantaneous wall stress and heat flux are related to the velocity and potential temperature, respectively, at the first vertical node through the application of the Monin-Obukhov similarity theory as follows [82]:

$$\tau_{i3}|_w = -u_*^2 \frac{\tilde{u}_i}{\tilde{u}_r} = -\left(\frac{\tilde{u}_r \kappa}{\ln(z/z_o) - \Psi_M}\right)^2 \frac{\tilde{u}_i}{\tilde{u}_r}, \quad q_3|_w = \frac{u_* \kappa(\theta_s - \tilde{\theta})}{\ln(z/z_{ot}) - \Psi_H}, \tag{A1}$$

where $\tau_{i3}|_w$ and $q_3|_w$ are the instantaneous local wall stress and heat flux, respectively; u_* is the friction velocity; z_o and z_{ot} are the surface roughness for momentum and potential temperature, respectively; κ is the von Kármán constant, $\tilde{u}_r$ is the local filtered horizontal velocity at the first level $z = \Delta_z/2$, and θ_s is the surface (ground level) potential temperature. $\Psi_M = -4.8z/L$ and $\Psi_H = -7.8z/L$ are the stability corrections for momentum and heat under the stably stratified condition, respectively, where $L = -(u_*^3\theta_0)/(\kappa g q_3|_w)$ is the local Obukhov length [83,84].

---

[1] L. J. Vermeer, J. N. Sørensen, and A. Crespo, Wind turbine wake aerodynamics, Prog. Aerosp. Sci. **39**, 467 (2003).
[2] M. Hansen, J. N. Sørensen, S. Voutsinas, N. Sørensen, and H. Madsen, State of the art in wind turbine aerodynamics and aeroelasticity, Prog. Aerosp. Sci. **42**, 285 (2006).
[3] B. Sanderse, S. P. Pijl, and B. Koren, Review of computational fluid dynamics for wind turbine wake aerodynamics, Wind Energy **14**, 799 (2011).
[4] J. N. Sørensen, Aerodynamic aspects of wind energy conversion, Annu. Rev. Fluid Mech. **43**, 427 (2011).
[5] D. Mehta, A. Van Zuijlen, B. Koren, J. Holierhoek, and H. Bijl, Large eddy simulation of wind farm aerodynamics: A review, J. Wind Eng. Ind. Aerodyn. **133**, 1 (2014).
[6] S. E. Larsen, S.-E. Gryning, N. Jensen, H. Jørgensen, and J. J. Mann, Mean wind and turbulence in the atmospheric boundary layer above the surface layer, in *Wind Energy* (Springer, Berlin, 2007), p. 21.
[7] R. J. Barthelmie, S. T. Frandsen, M. N. Nielsen, S. C. Pryor, P. E. Rethore, and H. E. Jørgensen, Modelling and measurements of power losses and turbulence intensity in wind turbine wakes at Middelgrunden offshore wind farm, Wind Energy **10**, 517 (2007).
[8] R. J. Barthelmie, S. C. Pryor, S. T. Frandsen, K. S. Hansen, J. G. Schepers, K. Rados, W. Schlez, A. Neubert, and L. E. Jensen, Quantifying the impact of wind turbine wakes on power output at offshore wind farms, J. Atmos. Oceanic Technol. **27**, 1302 (2010).
[9] R. J. Barthelmie and L. E. Jensen, Evaluation of wind farm efficiency and wind turbine wakes at the Nysted offshore wind farm, Wind Energy **13**, 573 (2010).
[10] K. S. Hansen, R. J. Barthelmie, L. E. Jensen, and A. Sommer, The impact of turbulence intensity and atmospheric stability on power deficits due to wind turbine wakes at Horns Rev wind farm, Wind Energy **15**, 183 (2012).
[11] M. J. Churchfield, S. Lee, P. J. Moriarty, Y. Hao, M. A. Lackner, R. Barthelmie, J. K. Lundquist, and G. Oxley, A comparison of the dynamic wake meandering model, large-eddy simulation, and field data at the Egmond aan Zee offshore wind plant, in *33rd Wind Energy Symposium*, AIAA SciTech, (AIAA 2015-0724), http://arc.aiaa.org/doi/abs/10.2514/6.2015-0724.
[12] J. P. Goit and J. Meyers, Optimal control of energy extraction in wind-farm boundary layers, J. Fluid Mech. **768**, 5 (2015).
[13] N. Troldborg, J. Sørensen, and R. Mikkelsen, Actuator line simulation of wake of wind turbine operating in turbulent inflow, J. Phys.: Conf. Ser. **75**, 012063 (2007).
[14] J. N. Sørensen, R. F. Mikkelsen, D. S. Henningson, S. Ivanell, S. Sarmast, and S. J. Andersen, Simulation of wind turbine wakes using the actuator line technique, Phil. Trans. R. Soc. A **373**, 20140071 (2015).
[15] H. Sarlak, C. Meneveau, and J. N. Sørensen, Role of subgrid-scale modeling in large eddy simulation of wind turbine wake interactions, Renewable Energy **77**, 386 (2015).

[16] L. Chamorro and F. Porté-Agel, A wind-tunnel investigation of wind turbine wakes: Boundary-layer turbulence effects, Boundary-Layer Meteorol. **132**, 129 (2009).

[17] R. B. Cal, J. Lebrón, L. Castillo, H. S. Kang, and C. Meneveau, Experimental study of the horizontally averaged flow structure in a model wind turbine array boundary layer, J. Renewable Sustainable Energy **2**, 013106 (2010).

[18] Y. T. Wu and F. Porté-Agel, Atmospheric turbulence effects on wind-turbine wakes: An LES study, Energies **5**, 5340 (2012).

[19] C. D. Markfort, W. Zhang, and F. Porté-Agel, Turbulent flow and scalar transport through and over aligned and staggered wind farms, J. Turbul. **13**, 1 (2012).

[20] N. Hamilton, H. S. Kang, C. Meneveau, and R. B. Cal, Statistical analysis of kinetic energy entrainment in a model wind turbine array boundary layer, J. Renewable Sustainable Energy **4**, 063105 (2012).

[21] L. Chamorro, C. Hill, S. Morton, C. Ellis, R. Arndt, and F. Sotiropoulos, On the interaction between a turbulent open channel flow and an axial-flow turbine, J. Fluid Mech. **716**, 658 (2013).

[22] G. V. Iungo, Y. T. Wu, and F. Porté-Agel, Field measurements of wind turbine wakes with lidars, J. Atmos. Oceanic Technol. **30**, 274 (2013).

[23] W. Tian, A. Ozbay, and H. Hu, Effects of incoming surface wind conditions on the wake characteristics and dynamic wind loads acting on a wind turbine model, Phys. Fluids **26**, 125108 (2014).

[24] G. Espana, S. Aubrun, S. Loyer, and P. Devinant, Wind tunnel study of the wake meandering downstream of a modelled wind turbine as an effect of large scale turbulent eddies, J. Wind Eng. Ind. Aerodyn. **101**, 24 (2012).

[25] R. E. Keck, M. Mare, J. M. Churchfield, S. Lee, and G. Larsen, On atmospheric stability in the dynamic wake meandering model, Wind Energy **17**, 1689 (2014).

[26] M. Abkar and F. Porté-Agel, Influence of atmospheric stability on wind turbine wakes: A large-eddy simulation study, Phys. Fluids **27**, 035104 (2015).

[27] K. Rados, G. Larsen, R. Barthelmie, W. Schlez, B. Lange, G. Schepers, T. Hegberg, and M. Magnisson, Comparison of wake models with data for offshore wind farms, Wind Eng. **25**, 271 (2001).

[28] P. E. Rethore, N. N. Sørensen, A. Bechmann, and F. Zahle, Study of the atmospheric wake turbulence of a CFD actuator disc model, in *Proceedings of European Wind Energy Conference, Marseille, France, 2009*.

[29] M. J. Churchfield, S. Lee, J. Michalakes, and P. J. Moriarty, A numerical study of the effects of atmospheric and wake turbine dynamics, J. Turbul. **13**, N14 (2012).

[30] M. L. Aitken, B. Kosović, J. D. Mirocha, and J. K. Lundquist, Large eddy simulation of wind turbine wake dynamics in the stable boundary layer using the weather research and forecasting model, J. Renewable Sustainable Energy **6**, 033137 (2014).

[31] J. D. Mirocha, D. A. Rajewski, N. Marjanovic, J. K. Lundquist, B. Kosović, C. Draxl, and M. J. Churchfield, Investigating wind turbine impacts on near-wake flow using profiling lidar data and large-eddy simulations with an actuator disk model, J. Renewable Sustainable Energy **7**, 043143 (2015).

[32] K. Bhaganagar and M. Debnath, The effects of mean atmospheric forcings of the stable atmospheric boundary layer on wind turbine wake, J. Renewable Sustainable Energy **7**, 013124 (2015).

[33] J. Lundquist, M. Churchfield, S. Lee, and A. Clifton, Quantifying error of lidar and sodar Doppler beam swinging measurements of wind turbine wakes using computational fluid dynamics, Atmos. Meas. Tech. **8**, 907 (2015).

[34] M. Bromm, L. Vollmer, and M. Kühn, Numerical investigation of wind turbine wake development in directionally sheared inflow, Wind Energy (2016), doi: 10.1002/we.2010.

[35] D. Medici and P. H. Alfredsson, Measurements on a wind turbine wake: 3d effects and bluff body vortex shedding, Wind Energy **9**, 219 (2006).

[36] T. Maeda, Y. Kamada, J. Murata, S. Yonekura, T. Ito, A. Okawa, and T. Kogaki, Wind tunnel study on wind and turbulence intensity profiles in wind turbine wake, J. Thermal Sci. **20**, 127 (2011).

[37] M. Magnusson and A. S. Smedman, Influence of atmospheric stability on wind turbine wakes, Wind Eng. **18**, 139 (1994).

[38] W. Zhang, C. D. Markfort, and F. Porté-Agel, Wind-turbine wakes in a convective boundary layer: A wind-tunnel study, Boundary-Layer Meteorol. **146**, 161 (2013).

[39] G. V. Iungo and F. Porté-Agel, Volumetric lidar scanning of wind turbine wakes under convective and neutral atmospheric stability regimes, J. Atmos. Oceanic Technol. **31**, 2035 (2014).
[40] P. E. Hancock and F. Pascheke, Wind-tunnel simulation of the wake of a large wind turbine in a stable boundary layer: Part 2, The wake flow, Boundary-Layer Meteorol. **151**, 23 (2014).
[41] M. L. Aitken, R. M. Banta, Y. L. Pichugina, and J. K. Lundquist, Quantifying wind turbine wake characteristics from scanning remote sensor data, J. Atmos. Oceanic Technol. **31**, 765 (2014).
[42] M. L. Aitken and J. K. Lundquist, Utility-scale wind turbine wake characterization using nacelle-based long-range scanning lidar, J. Atmos. Oceanic Technol. **31**, 1529 (2014).
[43] P. E. Hancock and S. Zhang, A wind-tunnel simulation of the wake of a large wind turbine in a weakly unstable boundary layer, Boundary-Layer Meteorol. **156**, 395 (2015).
[44] M. Dörenkämper, B. Witha, G. Steinfeld, D. Heinemann, and M. Kühn, The impact of stable atmospheric boundary layers on wind turbine wakes within offshore wind farms, J. Wind Eng. Ind. Aerodyn. **144**, 146 (2015).
[45] G. V. Iungo, Experimental characterization of wind turbine wakes: Wind tunnel tests and wind LiDAR measurements, J. Wind Eng. Ind. Aerodyn. **149**, 35 (2016).
[46] E. Machefaux, G. C. Larsen, T. Koblitz, N. Troldborg, M. C. Kelly, A. Chougule, K. S. Hansen, and J. S. Rodrigo, An experimental and numerical study of the atmospheric stability impact on wind turbine wakes, Wind Energy **19**, 1785 (2016).
[47] I. N. Esau and S. S. Zilitinkevich, Universal dependences between turbulent and mean flow parameters instably and neutrally stratified planetary boundary layers, Nonlin. Processes Geophys. **13**, 135 (2006).
[48] F. Zahle, N. Sørensen, and H. Madsen Aagaard, The influence of wind shear and tower presence on rotor and wake aerodynamics using CFD, in *Research in Aeroelasticity EFP-2007*, edited by C. Bak (Risø National Laboratory, Technical University of Denmark, Roskilde, Denmark, 2008), pp. 17–34.
[49] H. Lu and F. Porté-Agel, Large-eddy simulation of a very large wind farm in a stable atmospheric boundary layer, Phys. Fluids **23**, 065101 (2011).
[50] L. Vollmer, M. van Dooren, D. Trabucchi, J. Schneemann, G. Steinfeld, B. Witha, J. Trujillo, and M. Kuhn, First comparison of LES of an offshore wind turbine wake with dual-Doppler lidar measurements in a German offshore wind farm, J. Phys.: Conf. Ser. **625**, 012001 (2015).
[51] M. Abkar, A. Sharifi, and F. Porté-Agel, Wake flow in a wind farm during a diurnal cycle, J. Turbul. **17**, 420 (2016).
[52] D. Allaerts and J. Meyers, Effect of inversion-layer height and Coriolis forces on developing wind-farm boundary layers, in *34th Wind Energy Symposium*, AIAA SciTech, (AIAA 2016-1989), http://dx.doi.org/10.2514/6.2016-1989.
[53] F. Porté-Agel, Y. T. Wu, H. Lu, and R. J. Conzemius, Large-eddy simulation of atmospheric boundary layer flow through wind turbines and wind farms, J. Wind Eng. Ind. Aerodyn. **99**, 154 (2011).
[54] Y. T. Wu and F. Porté-Agel, Simulation of turbulent flow inside and above wind farms: Model validation and layout effects, Boundary-Layer Meteorol. **146**, 181 (2013).
[55] F. Porté-Agel, Y. T. Wu, and C. H. Chen, A numerical study of the effects of wind direction on turbine wakes and power losses in a large wind farm, Energies **6**, 5297 (2013).
[56] M. Abkar and F. Porté-Agel, The effect of free-atmosphere stratification on boundary-layer flow and power output from very large wind farms, Energies **6**, 2338 (2013).
[57] J. W. Deardorff, Three-dimensional numerical study of the height and mean structure of a heated planetary boundary layer, Boundary-Layer Meteorol. **7**, 81 (1974).
[58] R. Stoll and F. Porté-Agel, Dynamic subgrid-scale models for momentum and scalar fluxes in large-eddy simulations of neutrally stratified atmospheric boundary layers over heterogeneous terrain, Water Resour. Res. **42**, W01409 (2006).
[59] Y. T. Wu and F. Porté-Agel, Modeling turbine wakes and power losses within a wind farm using LES: An application to the Horns Rev offshore wind farm, Renewable Energy **75**, 945 (2015).
[60] Y. T. Wu and F. Porté-Agel, Large-eddy simulation of wind-turbine wakes: Evaluation of turbine parametrisations, Boundary-Layer Meteorol. **138**, 345 (2011).
[61] R. J. Beare, M. K. MacVean, A. A. M. Holtslag, J. Cuxart, I. Esau, J.-C. Golaz, M. A. Jimenez, M. Khairoutdinov, B. Kosovic, D. Lewellen, T. S. Lund, J. K. Lundquist, A. McCabe, A. F. Moene, Y. Noh,

S. Raasch, and P. Sullivan, An intercomparison of large-eddy simulations of the stable boundary layer, Boundary-Layer Meteorol. **118**, 247 (2006).
[62] A. Sescu and C. Meneveau, A control algorithm for statistically stationary large-eddy simulations of thermally stratified boundary layers, Q. J. R. Meteorol. Soc. **140**, 2017 (2014).
[63] M. Abkar and F. Porté-Agel, A new wind-farm parameterization for large-scale atmospheric models, J. Renewable Sustainable Energy **7**, 013121 (2015).
[64] D. Allaerts and J. Meyers, Large eddy simulation of a large wind-turbine array in a conventionally neutral atmospheric boundary layer, Phys. Fluids **27**, 065108 (2015).
[65] S. Zilitinkevich and I. Esau, The effect of baroclinicity on the depth of neutral and stable planetary boundary layers, Q. J. R. Meteorol. Soc. **129**, 3339 (2003).
[66] F. T. Nieuwstadt, The turbulent structure of the stable, nocturnal boundary layer, J. Atmos. Sci. **41**, 2202 (1984).
[67] F. T. Nieuwstadt, A model for the stationary, stable boundary layer, in *Turbulence and Diffusion in Stable Environments*, edited by J. C. R. Hunt (Oxford University, Oxford, 1985), p. 149.
[68] G. N. Coleman, J. H. Ferziger, and P. R. Spalart, Direct simulation of the stably stratified turbulent ekman layer, J. Fluid Mech. **244**, 677 (1992).
[69] B. Kosovic and J. A. Curry, A large eddy simulation study of a quasi-steady, stably stratified atmospheric boundary layer, J. Atmos. Sci. **57**, 1052 (2000).
[70] S. Basu and F. Porté-Agel, Large-eddy simulation of stably stratified atmospheric boundary layer turbulence: A scale-dependent dynamic modeling approach, J. Atmos. Sci. **63**, 2074 (2006).
[71] R. Stoll and F. Porté-Agel, Large-eddy simulation of the stable atmospheric boundary layer using dynamic models with different averaging schemes, Boundary-Layer Meteorol. **126**, 1 (2008).
[72] Y. H. Tseng, C. Meneveau, and M. B. Parlange, Modeling flow around bluff bodies and predicting urban dispersion using large eddy simulation, Environ. Sci. Technol. **40**, 2653 (2006).
[73] M. Abkar and F. Porté-Agel, A new boundary condition for large-eddy simulation of boundary-layer flow over surface roughness transitions, J. Turbul. **13**, N23 (2012).
[74] W. Munters, C. Meneveau, and J. Meyers, Turbulent inflow precursor method with time-varying direction for large-eddy simulations and applications to wind farms, Boundary-Layer Meteorol. **159**, 305 (2016).
[75] S. Xie and C. Archer, Self-similarity and turbulence characteristics of wind turbine wakes via large-eddy simulation, Wind Energy **18**, 1815 (2015).
[76] A. Rosen and Y. Sheinman, The power fluctuations of a wind turbine, J. Wind Eng. Ind. Aerodyn. **59**, 51 (1996).
[77] R. Johnstone and G. Coleman, The turbulent Ekman boundary layer over an infinite wind turbine array, J. Wind Eng. Ind. Aerodyn. **100**, 46 (2012).
[78] M. Abkar and F. Porté-Agel, Mean and turbulent kinetic energy budgets inside and above very large wind farms under conventionally-neutral condition, Renewable Energy **70**, 142 (2014).
[79] S. Pope, *Turbulent Flows* (Cambridge University, New York, 2000).
[80] S. A. Orszag, Transform method for calculation of vector coupled sums: Application to the spectral form of the vorticity equation, J. Atmos. Sci. **27**, 890 (1970).
[81] C. Canuto, M. Hussaini, A. Quarteroni, and T. Zang, *Spectral Methods in Fluid Dynamics* (Springer, Berlin, 1988).
[82] C. Moeng, A large-eddy simulation model for the study of planetary boundary-layer turbulence, J. Atmos. Sci. **46**, 2311 (1984).
[83] J. A. Businger, J. C. Wyngaard, Y. Izumi, and E. F. Bradley, Flux-profile relationships in the atmospheric surface layer, J. Atmos. Sci. **28**, 181 (1971).
[84] R. Stull, *An Introduction to Boundary-Layer Meteorology* (Kluwer Academic, Dordrecht, 1988).